Experimental postseismic recovery of fractured rocks assisted by calcite sealing

F. M. Aben[1,2] ⓘD, M.-L. Doan[1], J.-P. Gratier[1], and F. Renard[1,3] ⓘD

[1]University Grenoble Alpes and University Savoie Mont Blanc, CNRS, IRD, IFSTTAR, Grenoble, France, [2]Now at Department of Earth Sciences, University College London, London, UK, [3]Department of Geosciences, PGP, University of Oslo, Oslo, Norway

Abstract Postseismic recovery within fault damage zones involves slow healing of coseismic fractures leading to permeability reduction and strength increase with time. To better understand this process, experiments were performed by long-term fluid percolation with calcite precipitation through predamaged quartz-monzonite samples subjected to upper crustal conditions of stress and temperature. This resulted in a *P* wave velocity recovery of 50% of its initial drop after 64 days. In contrast, the permeability remained more or less constant for the duration of the experiment. Microstructures, fluid chemistry, and X-ray microtomography demonstrate that incipient calcite sealing and asperity dissolution are responsible for the *P* wave velocity recovery. The permeability is unaffected because calcite precipitates outside of the main flow channels. The highly nonparallel evolution of strength recovery and permeability suggests that fluid conduits within fault damage zones can remain open fluid conduits after an earthquake for much longer durations than suggested by the seismic monitoring of fault healing.

1. Introduction

Rock properties in upper crustal fault zones (down to 5 km depth) change during and after an earthquake, such as seismic velocities [*Peng and Ben-Zion*, 2006; *Kelly et al.*, 2013; *Olivier et al.*, 2015], fluid flow properties [*Yaltirak et al.*, 2005], and fluid composition [*Claesson et al.*, 2007]. After, in the postseismic and interseismic phase, these properties restore toward their preseismic state [*Li et al.*, 1998; *Peng and Ben-Zion*, 2006; *Claesson et al.*, 2007; *Brenguier et al.*, 2008; *Kelly et al.*, 2013; *Wästeby et al.*, 2014]. These changes are caused by earthquake-related fracture damage and postseismic healing or recovery of such damage. Such recovery causes the rock to strengthen, but it might also reduce permeability within the fault zone. Consequently, increasing pore fluid pressure leads to effective weakening of the fault [*Sibson*, 1990]. Moreover, within crustal fault zones, postseismic recovery may be correlated to transient postseismic creep [*Reilinger et al.*, 2000; *Lyons and Sandwell*, 2003; *Cakir et al.*, 2012]. Thus, postseismic and interseismic recovery of fault rocks in the upper crust is a complex interplay between mechanical, hydrological, and chemical processes that accommodate permanent strain and influence fault strength and the recurrence time of earthquakes [*Gratier and Gueydan*, 2007].

Contributions to postseismic healing come from both the fault core and the fault damage zone. In the fault core healing involves compaction of "loose" fragmented material and gouge by grain size dependent mechanisms that act relatively fast [e.g., *Renard et al.*, 2000; *Bos and Spiers*, 2002; *Tenthorey and Cox*, 2006; *Niemeijer et al.*, 2008; *Pluymakers et al.*, 2014; *Chen et al.*, 2015a, 2015b]. The fault core is therefore often considered as an impermeable barrier [*Sibson*, 1990; *Faulkner et al.*, 2010], except for a short period after a seismic event. By contrast, the fault damage zone can be considered as an elastic medium containing fractures; thus, the healing of these fractures controls the strengthening of the fault damage zone. Besides, the fault damage zone acts as a fluid conduit and affects the hydrological properties of the entire fault zone.

Therefore, it is vital to understand the healing process responsible for strengthening of the fractured medium while also understanding how the recovery process influences fluid flow in the fault zone. At least, four recovery mechanisms have been suggested.

1. Mechanical time-dependent recovery of microscale cracks by backsliding on wing crack geometries [*Brantut*, 2015]. Microscale pressure solution processes accompany the backsliding.

2. "Self-healing"—sometimes called "healing," not to be confused with the term healing for large-scale restrengthening or recovery—involves surface energy-driven closure of microscale cracks [e.g., *Brantley et al.*, 1990; *Brantley*, 1992].

3. Sealing by mineral precipitation, resulting in fracture sealing that often consist of calcite or quartz (experiments by, e.g., *Lee and Morse* [1999], *Morrow et al.* [2001] *Dobson et al.* [2003], and *Jones and Detwiler* [2016]). Deviatoric stress does not directly influence this mechanism, but deviatoric stress may indirectly cause fracture opening or closure.

4. Fracture closure by pressure solution creep. Here deviatoric stress causes local differences in the solubility of a material, causing local dissolution and precipitation. This also accommodates deformation at the grain scale [*Renard et al.*, 2000; *Gratier and Gueydan*, 2007; *Gratier et al.*, 2014].

The four mechanisms described above can occur simultaneously, and their dominance depends, among other parameters, on the size of the fractures [*Gratier and Gueydan*, 2007]. For instance, mechanisms (1) and (2) occur in small micrometric fractures at short time scales, while (3) and (4) can close fractures on centimeter-meter scale and act on longer time scales. All mechanisms are enhanced by, or necessitate the presence of, an aqueous fluid phase in the rock. To understand the full extent of postseismic recovery in the damage zone, each mechanism should be studied separately.

Here mechanism (3), sealing by precipitation, is targeted. The goal is to study the evolution and coupling of hydrological properties and mechanical strengthening during the sealing of a fracture network in a natural rock sample. To do so, laboratory experiments were performed on predamaged and microfractured quartz monzonite samples. The samples were subjected to prolonged percolation of a calcite-saturated fluid under upper crustal conditions. The fluid flow properties and the fluid chemistry were monitored during the experiment. X-ray microtomography scans and P wave velocity measurements were performed before and after the experiment. The obtained data set provides unique insights into the first stages of fracture sealing and the effect it has on the evolution of permeability and elastic properties after an earthquake.

2. Method

Quartz-monzonite was used as sample material (see *Aben et al.* [2016] for an extensive description of the material). The low porosity of the undamaged material (0.6–0.9%) ensures that any permeability can be ascribed to the introduced fracture damage. Two cylindrical samples (labeled QMP3 and QMP4) with a length and diameter of 2 cm were prepared. The ends were grinded parallel up to 0.006 mm before the samples were jacketed to prevent premature failure. Dynamically induced microfracture damage was created by uniaxial high strain rate loading using a "mini"-Split Hopkinson Pressure Bar at the ISTerre laboratory, Grenoble. A detailed description of the method and the specifications of this apparatus are provided in *Aben et al.* [2016]. The rock was subjected to successive loadings at relatively low stress (i.e., below the pulverization threshold) to ensure better control on the amount of damage, similarly to the experiments by *Aben et al.* [2016]. Such experiments result in a pervasive sample-wide fracture network without losing the cohesion of the rock and without accumulating of large amounts of shear along the fractures [*Aben et al.*, 2016]. For samples QMP3 and QMP4, such a well-defined sample-wide fracture network had been developed after three and eight successive loadings, respectively. The specific loading conditions of these loadings are given in supporting information Table S1.

The recovery experiments were performed at the ISTerre laboratory, Grenoble, in two triaxial pressure vessels (numbered cell 1 and cell 2) containing pore fluid systems connected to an autoclave and high-pressure liquid chromatography (HPLC) pump. For more details on these cells, see *Hellmann et al.* [2002], *Le Guen et al.* [2007], *Richard et al.* [2014a], and supporting information Text S2.

The duration of the healing experiments was 64 days, consisting of three phases: (1) dry loading for 7 days, (2) percolation of deionized water for 10 days, and (3) percolation of a calcite-saturated fluid for the remainder of the time. The confining pressure (10 MPa), axial stress (16 MPa), temperature (90–100°C), the flow rate of the HPLC pump (3 mL/h), and the downflow fluid pressure (3.9 MPa) were kept constant over time, while the upstream fluid pressure was allowed to vary for both cells individually. All of these conditions were continuously monitored over the course of the experiment. Because the HPLC pump and autoclave were connected to both cells in parallel, an extra mass flow meter was emplaced in between the autoclave and cell 2 to obtain individual flow rates for each cell. The permeability was calculated as follows:
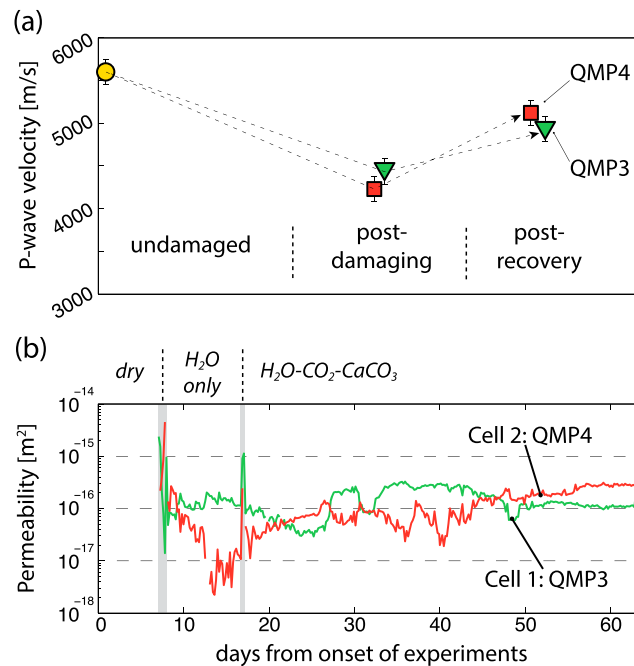
Figure 1. (a) *P* wave velocity measurements of the two tested samples before and after damaging, and after 64 days recovery. (b) Permeability measured in situ during the recovery experiments. The gray bars indicate the time change of the various stages of the experiment. The data are filtered to remove noise; see supporting information Text S2 for the raw data (mechanical data and hydrological data).

$$\kappa = \frac{Q\,\mu\,l}{A\,\Delta P}$$

where κ is the permeability (m^2), Q is the flow rate (m^3/s), μ is the dynamic viscosity (assumed constant and equal to 8.9×10^{-4} Pa s), l is the length of the sample (m), A is the surface area of the sample perpendicular to the flow (m^2), and ΔP is the difference between upstream and downstream fluid pressure (Pa).

The calcite-saturated fluid for phase 3 was continuously prepared in the autoclave system. The autoclave was filled with a sufficient amount of crushed and sieved Remollon calcite (grain size between 0.100 and 0.080 mm) and deionized water. The system was then pressurized using CO_2 gas, increasing the solubility of calcite. Deionized water was provided continuously by the HPLC pump, thereby forcing the calcite-saturated fluid into the samples. At regular intervals, extra CO_2 gas was added to ensure abundant CO_2 was present at the top of the autoclave.

The fluid, prepared at room temperature (20–25°C), was heated up within the triaxial cells (90–100°C). This caused a solubility drop of calcite, yielding calcite precipitation of up to 1.7 g/L [*Miller*, 1952; *Segnit et al.*, 1962; *Coto et al.*, 2012]. The fluid chemistry was measured regularly by inductively coupled plasma atomic emission spectroscopy analysis: every 1–2 weeks for autoclave fluids and every 2–3 days at the outlets of the cells.

Low-resolution X-ray computed tomography scans (voxel size 15 μm) were performed at the 3S-R laboratory, Grenoble, on both samples before and after the recovery experiment. In addition, one high-resolution scan (voxel size 2 μm) was obtained on postrecovery sample QMP3 at the beamline ID19 of the European Synchrotron Radiation Facility, Grenoble. The *P* wave velocity in each sample was measured before and after the recovery experiment, without confining pressure, and used as a proxy of damage [*Brantut*, 2015]. Finally, the samples were cut, their surface polished, and the microstructures were studied using a scanning electron microscopy (SEM).

3. Results

The *P* wave velocities measured had dropped from 5600 m/s to 4230 m/s (sample QMP4) and to 4450 m/s (sample QMP3) after fracture damage had been introduced (Figure 1a). The dissipated energy density, which corresponds to the amount of elastic strain energy transformed into new fractures during the successive loadings, was 0.35 and 0.65 MJ/m^3, respectively, for samples QMP4 and QMP3. The postrecovery velocities after the flow-through experiment show a significant increase from 4450 m/s to 4929 m/s (sample QMP3) and from 4230 m/s to 5120 m/s (sample QMP4) after 64 days (Figure 1a). This shows that the more damaged sample QMP3 has recovered less than the less damaged sample QMP4.

The mechanical and hydrological data are presented in detail in the supporting information Text S2. The permeability evolution over time was calculated from these data (see Figures 1b and S2 for a more detailed graph). The permeability of both samples was roughly similar, with an initial value of 10^{-16} m^2. The permeabilities varied within 1 order of magnitude over time, but we could not observe an unambiguous overall
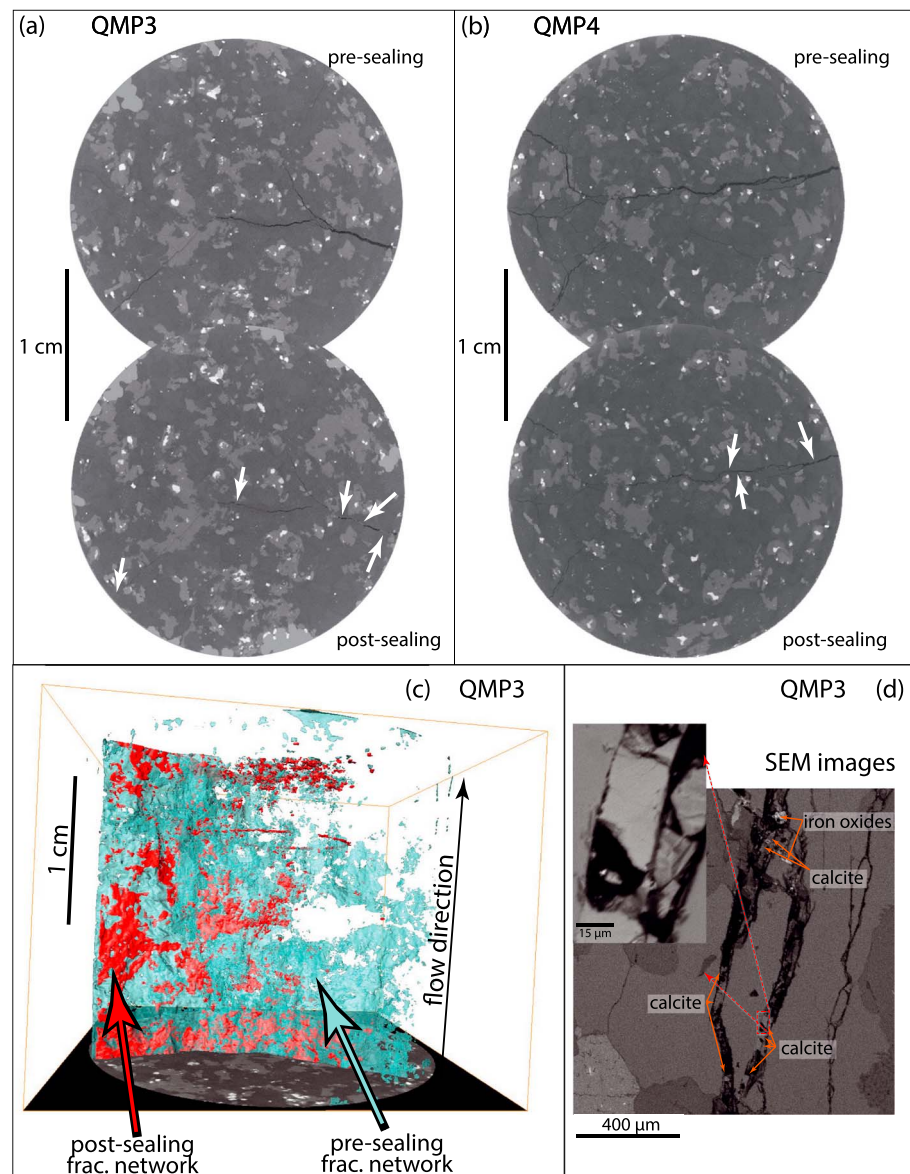
Figure 2. (a) X-ray microtomography 2-D images in sample QMP3, perpendicular to the loading and flow directions (top) before and (bottom) after the recovery flow through experiment. White arrows point to calcite sealing in the fractures. (b) X-ray microtomography 2-D images perpendicular to the loading and flow direction of sample QMP4, similar to Figure 2a. (c) Three-dimensional reconstruction of the open fracture volume in sample QMP3 before (blue) and after (red) the recovery experiment. Note the small rectangular holes in the red volume, caused by calcite patches. (d) SEM images of sample QMP3, perpendicular to the loading and flow directions. Fracture edges have been chipped because of polishing. Large euhedral calcite crystals are recognized in the main fractures, as well as iron oxide patches derived from the experimental system.

increase or decrease of permeability during damage recovery (Figure 1b). The permeability variations, due to fluctuations in the fluid pressure and flow rate, are caused by the setup (e.g., changing pure water percolation to calcite saturated fluid) and caused by temperature fluctuations in the laboratory [*Aben*, 2016]. High-frequency noise (either on the scale of hours or on seconds) is explained by degassing of the fluid, since CO_2 comes out of dissolution during the heating of the fluid.

The sample-sized fracture network is a volume revealed by the lower resolution X-ray tomography scans (Figures 2a–2c). During the recovery experiment, the individual sample-scale fractures have undergone a large decrease in fracture volume. The major contributor of the volume decrease was reduction of fracture aperture by mechanical closure. A smaller contribution came from small particles that form bridges or

props in the fracture volume, apparent in the larger fractures (Figures 2a and 2b). The high-resolution X-ray tomography data confirms that such particles are calcite precipitates that also partly fill fractures with smaller apertures (tomography images in Figure a). SEM images show that these particles are mostly euhedral calcite crystals (Figure 2d). The calcite patches often spans the whole fracture aperture, but their abundance is not sufficient to seal an entire fracture.

Partial calcite sealing does not occur randomly throughout the fracture network, in fact two geometric relations were observed: (1) preferential precipitation of calcite on certain mineral species of the host rock (e.g., pyroxene) and (2) a relation between calcite precipitation, fracture geometry, and macroscopic fluid flow. The first relation is illustrated by a major fracture that crosscuts a pyroxene grain (Figure 3a). Initially, the fracture aperture inside and outside this grain is similar. After the experiment, the fracture within the grain has been fully sealed. In contrast, the fracture outside this grain remained open.

The relationship between fracture geometry, macroscopic fluid flow, and partial sealing is best illustrated in 3-D reconstructions of the high-resolution tomography data. On the scale of individual fractures, calcite is observed near small fragments or props of the host rock that were displaced into the open fracture volume (Figure 3b). When the macroscopic flow direction is considered, it becomes apparent that the calcite crystals always precipitated downstream of such props. Similarly, calcite precipitated in narrow zones such as fracture steps and bends, as well as downstream of such flow barriers (Figure 3c). A somewhat larger-scale reconstruction shows that a more complex fracture system also facilitated precipitation of calcite (Figure 3d). At the bottom of this 3D reconstruction, calcite is scarce in fractures with a simple geometry. Toward the top, the fracture network becomes more complex where it terminates near a biotite grain. Steps, fragments and intersections are more abundant, as well as clusters of calcite crystals precipitating downstream of props and bottlenecks.

Chemical analyses reveal that the fluid at the outlet of the percolation system has been enriched with the elements K, Si, and in a lesser degree Na, relative to the injected fluid. This element signature was observed both during percolation of deionized water and of the calcite-rich fluid with CO_2. Over time, the dissolved amount of these species decreased slightly. After the onset of calcite-rich fluid percolation, the fluids within the autoclave and the outlets contained a large concentration of Ca, as well as larger concentrations of Sr and Mg. However, the data quality is not sufficient to calculate how much calcite has precipitated within the samples and to perform a full mass balance calculation. More detail on the fluid chemistry is provided in supporting information Figure S3.

4. Discussion: Healing Mechanisms and Permeability

The following interpretations are drawn from the data set presented above: (1) the samples have undergone recovery, as evidenced by the increase in P wave velocities (Figure 1a). (2) Fracture volume in the samples has decreased by permanent fracture closing and by calcite precipitation (Figure 2). (3) Permeability remained more or less constant over the course of the experiment (Figure 1b). This raises the key question why the permeability remained near stable, while the elastic constants of the rock recovered and the fracture volume decreased.

The increase in P wave velocities represents a proxy for bulk recovery of the samples. The recovery is attributed to the permanent closure of fractures, for which two contributions are identified: (i) the deformation and collapse of asperities on the fracture walls, either mechanically by local stress concentrations or chemically by dissolution and smoothing; and (ii): incipient calcite sealing of the fracture space.

Although deformation of asperities within the fractures is not supported by microstructural observations, dissolved K, Si, and in a lesser extent Na strongly suggest the dissolution of K-feldspar [*Busenberg and Clemency*, 1976] and possibly other minerals. The process of fracture closure by asperity dissolution has been observed by *Beeler and Hickman* [2004]. The rate of this process slows down nonlinearly over time, which is attributed to three mechanisms [*Beeler and Hickman*, 2004].

1. The first mechanism is the chemical potential of the fluid to dissolve chemical species from all free faces in the fracture. The dissolution rate decreases when the fluid reaches saturation of the chemical species, but also when the fresh feldspar surfaces are getting progressively weathered [*Busenberg and Clemency*, 1976; *Hellmann*, 1994]. Here continuous fluid flow reduces the effect of chemical saturation.
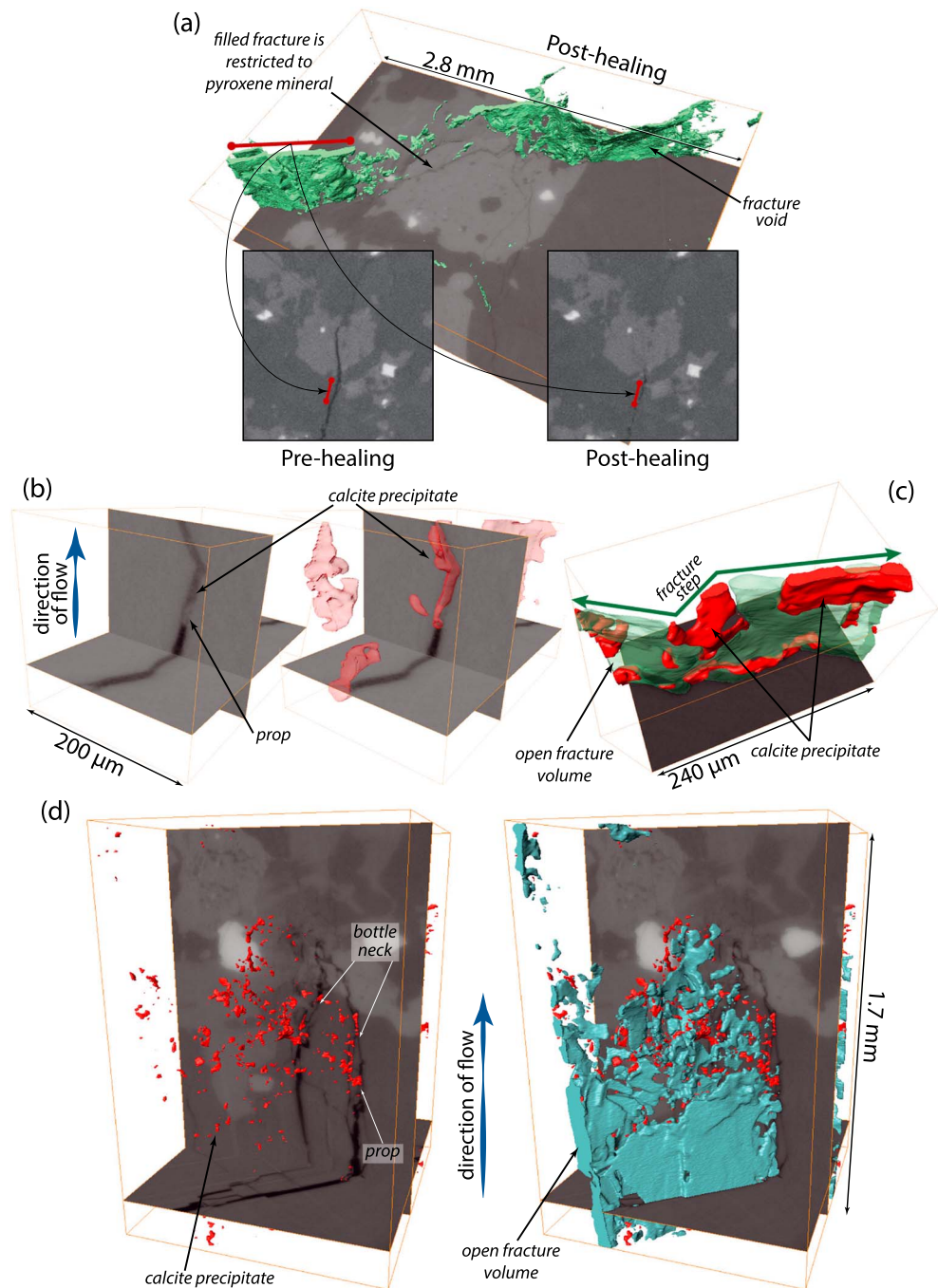
Figure 3. (a) Two-dimensional X-ray microtomography images (15 μm resolution) before and after sealing showing a fracture crossing a pyroxene grain. High-resolution (2 μm) 3-D reconstruction reveals that the postsealing fracture is open on both sides of the grain but is sealed within the grain. The red bar indicates the location of the same fracture interval in all three images. (b) High-resolution 3-D reconstruction showing the geometric relation between a prop in the fracture volume, precipitation of calcite, and the flow direction. (c) Three-dimensional reconstruction revealing precipitation of calcite within a relatively narrower fracture step. Same subvolume as Figure 3b. (d) Relation between flow direction, fracture geometry, and calcite deposition on a larger scale. Fracture geometry is straightforward at the bottom of the image; toward the top complexity increase and calcite precipitation are more abundant. Three-dimensional reconstruction from high-resolution tomography data.

2. The second mechanism is the coarsening potential or Ostwald ripening, driven by the minimization of surface energy. The contribution of this small-scale mechanism is minimal on the scale of the sample-traversing fractures.

3. The third mechanism is the pressure solution potential due to normal stress acting on the asperities and props. This causes a chemical potential gradient between free and stressed surfaces of the asperities that can, however, slow down over time by roughness reduction and contact area increase.

Recovery of the P wave velocity is also attributed to the formation of calcite precipitates (Figure 2) which often form in fracture steps (Figures 3c and 3d). Most fractures are parallel to the axes of the cylindrical sample, which is similar to the measurement direction of the P waves. Thus, parts of the fracture steps are oriented at an angle to the wave path. Such kinks, and the sealing of them, have a larger influence on the P wave velocity than parallel oriented fractures.

The contribution to the P wave velocity recovery of the other three recovery mechanisms proposed in section 1 (mechanical backsliding, self-healing and pressure solution) should be assessed as well. The relatively low temperature in combination with the rock mineralogy rules out a widespread contribution of pressure solution. Besides, supporting microstructural evidence is lacking. However, mechanical backsliding [*Brantut*, 2015] and self-healing of microscale fractures [*Brantley et al.*, 1990; *Brantley*, 1992] might occur pervasively and therefore contribute significantly to the P wave velocity reduction. Again, microstructural evidence is lacking, but it cannot be ruled out neither since the microfractures might be smaller than the resolution of the microtomography scans. This illustrates that the various healing mechanisms cannot be fully isolated from each other in recovery experiments on natural rock samples, and that recovery of damaged rocks in nature is a complex interplay between various healing mechanisms.

Nonetheless, we propose two conceptual mechanisms to explain why the permeability remained more or less constant while fracture volume was reduced: the location at which the calcite precipitates and the competition between dissolution of asperities and the growth of calcite.

4.1. The Location of Calcite Precipitation Within the Fracture

Irregularities within the fracture space, such as props, kinks, and bends (Figures 3b–3d), cause a heterogeneous distribution of the fluid flow through the fracture space. The fluid flow velocity is lower within and downstream of these regions. Hence, the contribution of these sheltered regions to the overall permeability of the fracture network is low. Thus, calcite that precipitates within these regions does not contribute much to the permeability reduction (Figure 4a).

The geometric relation between sheltered regions, main fluid flow pathways, and precipitation of a solid phase (Figure 4a) has been observed previously. For instance, computer simulations of calcite precipitation in a Berea sandstone show that precipitation occurred in low fluid flow zones in pores, adjacent to the main flow path traversing the pore [*Jiang and Tsuji*, 2014]. Experiments where calcite precipitated in a single fracture plane showed that the largest calcite patches precipitated adjacent to the preferential main fluid flow pathways [*Jones and Detwiler*, 2016]. Precipitation rates were much lower within the main flow path, effectively inhibiting complete sealing of the fracture. Hence, the location of precipitation is controlled by the trade-off between advection (i.e., the flux of chemical species carried by the fluid flow) and diffusion of the chemical species toward the precipitating mineral. As a consequence, the permeability does not change.

However, in the experiments performed by [*Jones and Detwiler*, 2016] the precipitation of calcite and the preferential fluid flow pathways were controlled by predetermined small-scale reaction sites on the fracture plane. These reaction sites consisted of pre-experimental calcite. Other sealing experiments in simpler geometries contain similar seeding locations [*Hilgers and Urai*, 2002; *Nollet et al.*, 2006; *Noiriel et al.*, 2012]. Epitaxial precipitation on a seeding location is energetically favorable over nucleating new crystals on other surfaces [*Teng et al.*, 2000]. Epitaxial growth and nucleation of new crystals occur simultaneously only when supersaturation in a fluid is very high [*Teng et al.*, 2000; *Noiriel et al.*, 2012]. Initially present calcite crystals are lacking in our samples, although some minerals act as a preferential seeding location (Figure 3a). Therefore, the location of precipitation is mostly determined by the trade-off between advection and diffusion (Figures 3b–3d).

4.2. Competition between Asperity Dissolution and Calcite Growth

The fracture aperture decreases over time by, among others, dissolution of props and asperities. However, incipient calcite precipitation competes with fracture closure as follows. Initially, the fracture is kept open by the props and asperities (Figure 4b, step 1). These props and asperities are slowly dissolved, while their
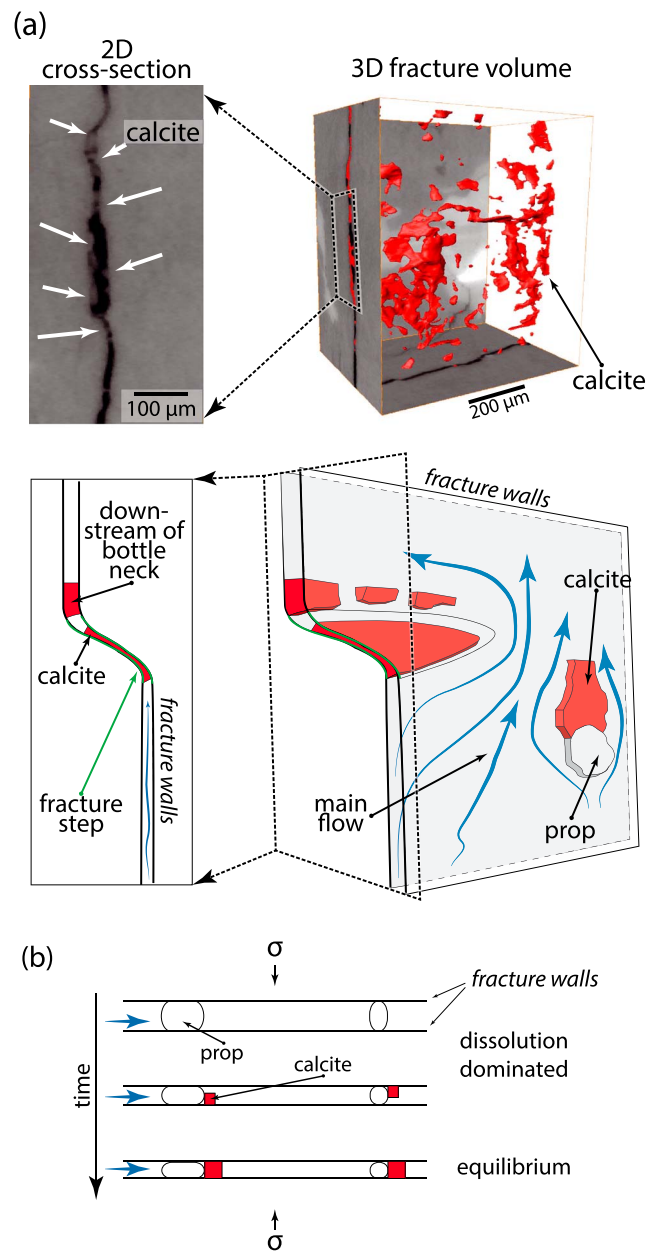
Figure 4. (a) High-resolution tomography images and simplified interpretations showing (left) a 2-D cross section of a fracture and (right) a 3-D fracture volume. Calcite patches are highlighted by the white arrows (2-D tomography image) and by the red volumes (3-D tomography reconstruction). In the sketch, calcite precipitations are highlighted in red as well. Flow barriers like fracture steps and props reduce the local fracture aperture, forcing the main flow around it. This causes a zone of reduced flow instream and downstream of the barrier. (b) The competition between prop or asperity dissolution and calcite growth in a cross section of a fracture. The first two time steps show dissolution dominated fracture closing. The third step shows calcite crystals large enough to adopt the role of the props, slowing down or inhibiting further closure of the fracture.

role is adopted by the calcite crystals growing in their flow shadow (Figure 4 b, steps 2 and 3). The calcite crystals cause the fracture to remain open, and they relieve the stress on the asperities, which slows down their dissolution.

If the recovery would continue beyond the duration of the experiment, the fractures would continue to be sealed by calcite. It is suspected that this will eventually cause the fracture space to become more and more compartmentalized and eventually the percolation threshold will be approached. Thus, the strength recovery of fractured rock is faster and more gradual over time relative to the permeability evolution, which could be more abrupt later in time.

5. Discussion: Implications for Postseismic Fault Strength Recovery

The upscaling of the recovery rates—in the order of months—presented here necessitates some discussion regarding the experimental conditions. The mechanical loading conditions and pore fluid pressures are realistic values for upper crustal conditions (10 MPa confining pressure equals roughly a depth of 350 m). The presence of CO_2 and dissolved calcite depends on the specific geological setting of a fault; nonetheless, some studies show fault zones that have been penetrated with CO_2-rich fluids [*Miller et al.*, 2004; *Smith et al.*, 2008]. However, the degree of oversaturation of calcite that was imposed in the experiment is much larger than in natural fault zones. Therefore, the recovery rate by calcite sealing is overestimated and will be in the order of years to decades rather than months. Timescales in the order of years to decades for postseismic recovery are similar to recovery rates in shallow fault zones, obtained by geochemistry [*Claesson et al.*, 2007; *Wästeby et al.*, 2014] and from seismological observations [*Li et al.*, 1998, 2003; *Li and Vidale*, 2001].

The experimental results suggest that seismic velocities are a poor proxy of postseismic recovery of a fault zone. Even if the seismic velocity returns to its pre-earthquake value in a few months [e.g., *Brenguier et al.*,

2008], a fault damage zone remains an open fluid conduit for much longer, for instance, during the first few years after a seismic event, since incipient fracture sealing by mineral precipitation causes progressive strengthening that is not accompanied with a parallel reduction of permeability. It should be noted that the relationship between postseismic strengthening and permeability could be different if another recovery mechanism is dominant instead of sealing, such as pressure solution. In such case, the recovery rate would depend on the composition of the lithology and pore fluids. For relatively large size fractures within a fault damage zone, sealing by fluid flow reproduced in this study is the most representative mechanism for what happens in nature. The resulting fluid flow, lasting several years after an earthquake, probably contributes to the long-term progressive weakening of fault gouge by activating fluid reactions leading to the development of clays [e.g., *Richard et al.*, 2014b]. Conversely, upper crustal fault damage zone would remain a conduit to dissipate pressurized fluids at depth for a longer duration as well.

6. Conclusion

Experiments performed in this study were designed to mimic part of the seismic cycle: first, coseismic damaging resulted in a sample-traversing fracture network. This results in a decrease in *P* wave velocity (Figure 1a). Next, postseismic recovery was achieved by exposing the sample to percolation of calcite-saturated fluids for 2 months, under upper crustal conditions. Recovery was measured as an increase in the *P* wave velocity after the experiment (Figure 1a). Two recovery mechanisms are proposed: mechanochemical reduction of the fracture aperture caused by dissolution and collapse of asperities, and the precipitation of calcite within the fracture space, leading to incipient sealing (Figure 2). Permeability, however, remained more or less constant during the recovery experiment (Figure 1b). This is attributed to two effects. On the one hand, the stress-supporting role of calcite crystals slows down the reduction of the fracture aperture (Figure 4b). On the other hand, calcite tends to precipitate in zones of the fracture volume away from the main flow path leading to only small changes in the overall permeability of the system (Figures 3 and 4a). These results suggest that seismic velocity measurements on postseismic recovery of fault zones do not constrain the reduction of permeability very well, and upper crustal fault zones (<5 km depth) can remain open conduits for fluids for a longer duration after a seismic event.

References

Aben, F. M. (2016) Experimental simulation of the seismic cycle in fault damage zones, PhD thesis, Univ. Grenoble Alpes. [Available at https://tel.archives-ouvertes.fr/tel-01528568/document].

Aben, F. M., M.-L. Doan, T. M. Mitchell, R. Toussaint, T. Reuschlé, M. Fondriest, J.-P. Gratier, and F. Renard (2016), Dynamic fracturing by successive coseismic loadings leads to pulverization in active fault zones, *J. Geophys. Res. Solid Earth*, *121*, 2338–2360, doi:10.1002/2015JB012542.

Beeler, N. M., and S. H. Hickman (2004), Stress-induced, time-dependent fracture closure at hydrothermal conditions, *J. Geophys. Res.*, *109*(B2), B02211, doi:10.1029/2002JB001782.

Bos, B., and C. J. Spiers (2002), Fluid-assisted healing processes in gouge-bearing faults: Insights from experiments on a rock analogue system, *Pure Appl. Geophys.*, *159*, 2537–2566, doi:10.1007/s00024-002-8747-2.

Brantley, S. L. (1992), The effect of fluid chemistry on quartz microcrack lifetimes, *Earth Planet Sci. Lett.*, *113*, 145–156.

Brantley, S. L., B. Evans, S. H. Hickman, and D. A. Crerar (1990), Healing in microcracks in quartz: Implications for fluid flow, *Geology*, *18*(2), 136–139.

Brantut, N. (2015), Time-dependent recovery of microcrack damage and seismic wave speeds in deformed limestone, *J. Geophys. Res. Solid Earth*, *120*, 8088–8109, doi:10.1002/2015JB012324.

Brenguier, F., M. Campillo, C. Hadziioannou, N. M. Shapiro, R. M. Nadeau, and E. Larose (2008), Postseismic relaxation along the San Andreas Fault at Parkfield from continuous seismological observations, *Science*, *321*(80), 1478–1481, doi:10.1126/science.1160943.

Busenberg, E., and C. V. Clemency (1976), The dissolution kinetics of feldspars at 25°C and 1 atm CO_2 partial pressure, *Geochim. Cosmochim. Acta*, *40*(1), 41–49, doi:10.1016/0016-7037(76)90192-7.

Cakir, Z., S. Ergintav, H. Ozener, U. Dogan, A. M. Akoglu, M. Meghraoui, and R. E. Reilinger (2012), Onset of aseismic creep on major strike-slip faults, *Geology*, *40*(12), 1115–1118, doi:10.1130/G33522.1. [Available at http://geology.gsapubs.org/cgi/doi/10.1130/G33522.1, accessed 1 October 2013.]

Chen, J., B. A. Verberne, and C. J. Spiers (2015a), Effects of healing on the seismogenic potential of carbonate fault rocks: Experiments on samples from the Longmenshan Fault, Sichuan, China, *J. Geophys. Res. Solid Earth*, *120*, 5479–5506, doi:10.1002/2015JB012051.

Chen, J., B. A. Verberne, and C. J. Spiers (2015b), Interseismic re-strengthening and stabilization of carbonate faults by "non-Dieterich" healing under hydrothermal conditions, *Earth Planet Sci. Lett.*, *423*, 1–12, doi:10.1016/j.epsl.2015.03.044.

Claesson, L., A. Skelton, C. Graham, and C.-M. Mörth (2007), The timescale and mechanisms of fault sealing and water-rock interaction after an earthquake, *Geofluids*, *7*(4), 427–440, doi:10.1111/j.1468-8123.2007.00197.x.

Coto, B., C. Martos, J. L. Peña, R. Rodríguez, and G. Pastor (2012), Effects in the solubility of $CaCO_3$: Experimental study and model description, *Fluid Phase Equilib.*, *324*, 1–7, doi:10.1016/j.fluid.2012.03.020.

Dobson, P. F., T. J. Kneafsey, E. L. Sonnenthal, N. Spycher, and J. A. Apps (2003), Experimental and numerical simulation of dissolution and precipitation: Implications for fracture sealing at Yucca Mountain, Nevada, *J. Contam. Hydrol.*, *62–63*, 459–476, doi:10.1016/S0169-7722(02)00155-9.

Faulkner, D. R., C. A. L. Jackson, R. J. Lunn, R. W. Schlische, Z. K. Shipton, C. A. J. Wibberley, and M. O. Withjack (2010), A review of recent developments concerning the structure, mechanics and fluid flow properties of fault zones, *J. Struct. Geol.*, *32*(11), 1557–1575, doi:10.1016/j.jsg.2010.06.009.

Gratier, J.-P., and and F. Gueydan (2007), Deformation in the presence of fluids and minerals: Effect of fracturing and fluid-rock interaction on seismic cycles, in *Tectonic Faults: Agents of Change on a Dynamic Earth*, 95, edited by M. R. Handy, G. Hirth, and N. Hovius, pp. 319–356, Dahlem Univ. Press., London, U. K.

Gratier, J.-P., F. Renard, and B. Vial (2014), Postseismic pressure solution creep: Evidence and time-dependent change from dynamic indenting experiments, *J. Geophys. Res. Solid Earth*, *119*, 2764–2779, doi:10.1002/2013JB010768.

Hellmann, R. (1994), The albite-water system: Part I. The kinetics of dissolution as a function of pH at 100, 200 and 300°C, *Geochim. Cosmochim. Acta*, *58*(2), 595–611, doi:10.1016/0016-7037(95)00075-B.

Hellmann, R., P. Gaviglio, P. J. N. Renders, J.-P. Gratier, S. Békri, and P. Adler (2002), Experimental pressure solution compaction of chalk in aqueous solutions Part 1. Deformation behavior and chemistry, in *Water-Rock Interact, Ore Deposits, Environmental Geochemistry: A Tribute to David A. Crerar*, vol. 7, pp. 153–178, Geochem. Soc., St. Louis, Mo.

Hilgers, C., and J. L. Urai (2002), Experimental study of syntaxial vein growth during lateral fluid flow in transmitted light: First results, *J. Struct. Geol.*, *24*(6–7), 1029–1043, doi:10.1016/S0191-8141(01)00089-X.

Jiang, F., and T. Tsuji (2014), Changes in pore geometry and relative permeability caused by carbonate precipitation in porous media, *Phys. Rev. E: Stat. Nonlinear, Soft Matter Phys.*, *90*(5), 1–10, doi:10.1103/PhysRevE.90.053306.

Jones, T. A., and R. L. Detwiler (2016), Fracture sealing by mineral precipitation: The role of small-scale mineral heterogeneity, *Geophys. Res. Lett.*, *43*, 7564–7571, doi:10.1002/2016GL069598.

Kelly, C. M., A. Rietbrock, D. R. Faulkner, and R. M. Nadeau (2013), Temporal changes in attenuation associated with the 2004 M6.0 Parkfield earthquake, *J. Geophys. Res. Solid Earth*, *118*, 630–645, doi:10.1002/jgrb.50088.

Lee, Y.-J., and J. W. Morse (1999), Calcite precipitation in synthetic veins: Implications for the time and fluid volume necessary for vein filling, *Chem. Geol.*, *156*(1–4), 151–170, doi:10.1016/S0009-2541(98)00183-1.

Le Guen, Y., F. Renard, R. Hellmann, E. Brosse, M. Collombet, D. Tisserand, and J.-P. Gratier (2007), Enhanced deformation of limestone and sandstone in the presence of high P_{CO_2} fluids, *J. Geophys. Res.*, *112*, B05421, doi:10.1029/2006JB004637.

Li, Y.-G., and J. E. Vidale (2001), Healing of the shallow fault zone from 1994–1998 after the 1992 M7.5 Landers, California, earthquake, *Geophys. Res. Lett.*, *28*(15), 2999–3002, doi:10.1029/2001GL012922.

Li, Y.-G., J. E. Vidale, K. Aki, F. Xu, and T. Burdette (1998), Evidence of shallow fault zone strengthening after the 1992 *M*7.5 Landers, California, earthquake, *Science*, *279*(5348), 217–219, doi:10.1126/science.279.5348.217.

Li, Y. G., J. E. Vidale, S. M. Day, D. D. Oglesby, and E. Cochran (2003), Postseismic fault healing on the rupture zone of the 1999 M 7.1 Hector Mine, California, earthquake, *Bull. Seismol. Soc. Am.*, *93*(2), 854–869, doi:10.1785/0120020131.

Lyons, S., and D. Sandwell (2003), Fault creep along the southern San Andreas from interferometric synthetic aperture radar, permanent scatterers, and stacking, *J. Geophys. Res. Earth*, *108*(B1), 2047, doi:10.1029/2002JB001831.

Miller, J. P. (1952), A portion of the system calcium carbonate-carbon dioxide-water, with geological implications, *Am. J. Sci.*, *250*, 161–203, doi:10.2475/ajs.250.3.161.

Miller, S. A., C. Collettini, L. Chiaraluce, M. Cocco, M. Barchi, and B. J. P. Kaus (2004), Aftershocks driven by a high-pressure CO_2 source at depth, *Nature*, *427*(6976), 724–727, doi:10.1038/nature02251.

Morrow, C. A., D. E. Moore, and D. A. Lockner (2001), Permeability reduction in granite under hydrothermal conditions, *J. Geophys. Res.*, *106*(B12), 30551–30560, doi:10.1029/2000JB000010.

Niemeijer, A., C. Marone, and D. Elsworth (2008), Healing of simulated fault gouges aided by pressure solution: Results from rock analogue experiments, *J. Geophys. Res.*, *113*, B04204, doi:10.1029/2007JB005376.

Noiriel, C., C. I. Steefel, L. Yang, and J. Ajo-Franklin (2012), Upscaling calcium carbonate precipitation rates from pore to continuum scale, *Chem. Geol.*, *318–319*, 60–74, doi:10.1016/j.chemgeo.2012.05.014.

Nollet, S., C. Hilgers, and J. L. Urai (2006), Experimental study of polycrystal growth from an advecting supersaturated fluid in a model fracture, *Geofluids*, *6*(2), 185–200, doi:10.1111/j.1468-8123.2006.00142.x.

Olivier, G., F. Brenguier, M. Campillo, P. Roux, N. M. Shapiro, and R. Lynch (2015), Investigation of coseismic and postseismic processes using in situ measurements of seismic velocity variations in an underground mine, *Geophys. Res. Lett.*, *42*, 9261–9269, doi:10.1002/2015GL065975.

Peng, Z., and Y. Ben-Zion (2006), Temporal changes of shallow seismic velocity around the Karadere-Düzce branch of the north Anatolian fault and strong ground motion, *Pure Appl. Geophys.*, *163*(2–3), 567–600, doi:10.1007/s00024-005-0034-6. [Available at http://link.springer.com/10.1007/s00024-005-0034-6, accessed 1 October 2013.]

Pluymakers, A. M. H., J. E. Samuelson, A. R. Niemeijer, and C. J. Spiers (2014), Effects of temperature and CO_2 on the frictional behavior of simulated anhydrite fault rock, *J. Geophys. Res. Solid Earth*, *119*, 8728–8747, doi:10.1002/2014JB011575.

Reilinger, R. E., et al. (2000), Coseismic and postseismic fault slip for the 17 August 1999, M=7.5, Izmit, Turkey, earthquake, *Science*, *289*(5484), 1519–1524, doi:10.1126/science.289.5484.1519.

Renard, F., J.-P. Gratier, and B. Jamtveit (2000), Kinetics of crack-sealing, intergranular pressure solution, and compaction around active faults, *J. Struct. Geol.*, *22*(10), 1395–1407, doi:10.1016/S0191-8141(00)00064-X.

Richard, J., M.-L. Doan, J.-P. Gratier, and F. Renard (2014a), Microstructures induced in porous limestone by dynamic loading, and fracture healing: An experimental approach, *Pure Appl. Geophys.*, doi:10.1007/s00024-014-0958-9. [Available at http://link.springer.com/10.1007/s00024-014-0958-9.]

Richard, J., J.-P. Gratier, M.-L. Doan, A.-M. Boullier, and F. Renard (2014b), Rock and mineral transformations in a fault zone leading to permanent creep: Interactions between brittle and viscous mechanisms in the San Andreas Fault, *J. Geophys. Res. Solid Earth*, *119*, 8132–8153, doi:10.1002/2014JB011489.

Segnit, E. R., H. D. Holland, and C. J. Biscardi (1962), The solubility of calcite in aqueous solutions—I the solubility of calcite in water between 75° and 200° at CO_2 pressures up to 60 atm, *Geochim. Cosmochim. Acta*, *26*, 1301–1331, doi:10.1016/0016-7037(62)90057-1.

Sibson, R. H. (1990), Conditions for fault-valve behaviour, *Geol. Soc. London, Spec. Publ.*, (54), 15–28.

Smith, S. A. F., C. Collettini, and R. E. Holdsworth (2008), Recognizing the seismic cycle along ancient faults: CO2-induced fluidization of breccias in the footwall of a sealing low-angle normal fault, *J. Struct. Geol.*, *30*(8), 1034–1046, doi:10.1016/j.jsg.2008.04.010.

Teng, H. H., P. M. Dove, and J. J. De Yoreo (2000), Kinetics of calcite growth: Surface processes and relationships to macroscopic rate laws, *Geochim. Cosmochim. Acta*, *64*(13), 2255–2266, doi:10.1016/S0016-7037(00)00341-0.

Tenthorey, E., and S. F. Cox (2006), Cohesive strengthening of fault zones during the interseismic period: An experimental study, *J. Geophys. Res.*, *111*, B09202, doi:10.1029/2005JB004122.

Wästeby, N., A. Skelton, E. Tollefsen, M. Andrén, G. Stockmann, L. C. Liljedahl, E. Sturkell, and M. Mörth (2014), Hydrochemical monitoring, petrological observation, and geochemical modeling of fault healing after an earthquake, *J. Geophys. Res. Solid Earth*, *119*, 5727–5740, doi:10.1002/2013JB010715.

Yaltirak, C., T. Yalçin, G. Yüce, and E. Bozkurtoglu (2005), Water-level changes in shallow wells before and after the 1999 Izmit and Düzce earthquakes and comparison with long-term water-level observations (1999–2004), NW Turkey, *Turkish J. Earth Sci.*, *14*, 281–309.